

Universal superconducting and magnetic properties of the $(\text{Ca}_x\text{La}_{1-x})(\text{Ba}_{1.75-x}\text{La}_{0.25+x})\text{Cu}_3\text{O}_y$ system: a μSR investigation

¹Amit Keren, ¹Amit Kanigel, ²James S. Lord, and ³Alex Amato

¹Physics Department, Technion-Israel Institute of Technology, Haifa 32000, Israel.

²Rutherford Appleton Laboratory, Chilton Didcot, Oxfordshire OX11 0QX, U.K.

³Paul Scherrer Institute, CH 5232 Villigen PSI, Switzerland

(November 1, 2018)

The $(\text{Ca}_x\text{La}_{1-x})(\text{Ba}_{1.75-x}\text{La}_{0.25+x})\text{Cu}_3\text{O}_y$ system is ideal for testing theories of high temperature superconductivity, since nearly the full range of doping is controlled by y , and T_c^{max} is continuously controlled by x , with minimal structural changes. We investigate this system with both transverse and longitudinal field μSR . This allows us to re-examine the Uemura relation, the nature of the spontaneous magnetic fields below T_c , and the relation between their appearance temperature T_g and T_c^{max} . Our major findings are: (I) the Uemura relation is respected by CLBLCO more adequately than by other cuprates, (II) T_g and T_c are controlled by the same energy scale, (III) the phase separation between hole poor and hole rich regions is a *microscopic* one, and (IV) spontaneous magnetic fields appear gradually with no moment size evolution.

The Uemura relation is a milestone in the research of high temperature superconductors [HTSC] and a key ingredient in most modern theories of HTSC. This relation¹ states that in underdoped HTSC the superconductivity transition temperature T_c is proportional to the muon spin rotation [μSR] line width σ , and that the proportionality constant is universal for all HTSC materials. Since σ is proportional to λ_{ab}^{-2} , where λ_{ab} is the in-plane penetration depth [see Sec. II], there is a one to one relation between T_c and λ_{ab}^{-2} for all underdoped HTSC. However, this relation seems to break in the optimally and overdoped regions. To date, the origin of this breakdown is not clear.

Another key ingredient of modern theories of HTSC is that at low temperatures (T), cuprates phase-separate into regions that are hole “poor” and hole “rich”². While hole rich regions become superconducting below T_c , the behavior of hole poor regions at these temperatures is not quite clear. Some data support the existence of magnetic moments in these regions³, but there are still many open questions regarding these moments and the spontaneous magnetic fields associated with them. For example: Is there a true phase transition at T_g ? What is the field profile and how is it different from, or similar to, a canonical spin glass? Is the field confined solely to the hole poor regions or does it penetrate the hole rich regions? Also, the interplay between magnetism and superconductivity is not clear. Is strong magnetic background beneficial or detrimental to superconductivity?

We address these questions by investigating the $(\text{Ca}_x\text{La}_{1-x})(\text{Ba}_{1.75-x}\text{La}_{0.25+x})\text{Cu}_3\text{O}_y$ (CLBLCO) family of superconductors. These superconductors belong to the 1:2:3 family and has several properties that make it ideal for our purpose. It is tetragonal throughout its range of existence $0 \leq x < 0.5$, so there is no ordering of CuO chains. Simple valence sums⁴, more sophisticated bond-valance calculations⁵, and thermoelectric power measurements⁶ show that the hole concentration is x independent. As shown in Fig. 1, by changing y , for

a constant value of x , the full superconductivity curve, from the underdoped to the overdoped, can be obtained. Finally, for different Ca contents, parallel curves of T_c vs y are generated. Therefore, with CLBLCO one can move continuously, and with minimal structural changes, from a superconductor resembling YBCO to one similar to LSCO. We study the superconducting and magnetic properties of CLBLCO by performing, zero, longitudinal, and transverse field muon spin relaxation experiments. The report on the zero and longitudinal field measurements is an extension of our recent letter⁷.

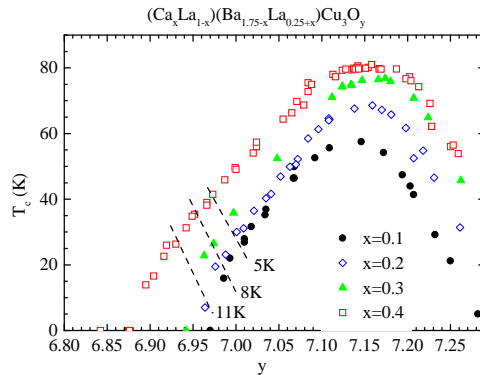


FIG. 1. Phase diagram of $(\text{Ca}_x\text{La}_{1-x})(\text{Ba}_{1.75-x}\text{La}_{0.25+x})\text{Cu}_3\text{O}_y$. The dashed lines indicate samples with equal T_g .

I. EXPERIMENTAL ASPECTS

The preparation of the samples is described elsewhere⁸. Oxygen content was determined using iodometric titration. All the samples were characterized using X-ray diffraction and were found to be single phase. T_c presented in the phase diagram is obtained from resistivity measurements.

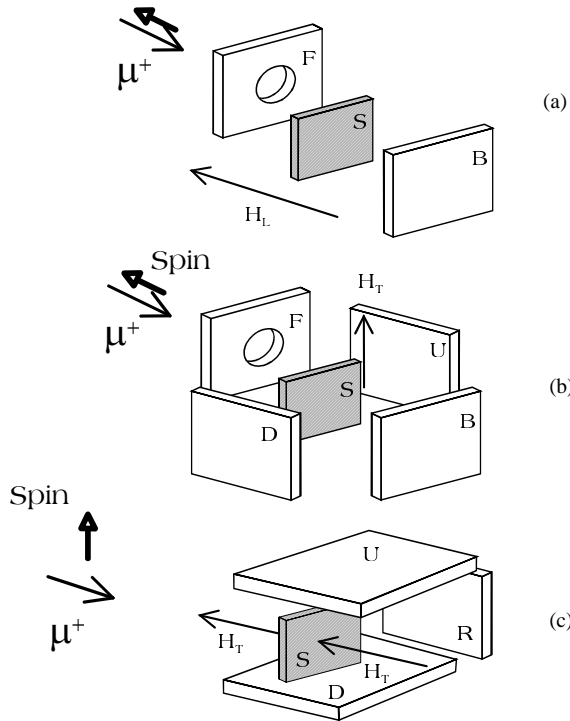


FIG. 2. μ SR experimental setup representing the (a) longitudinal and transverse field configurations in the (b) ISIS and (c) PSI facilities.

Our μ SR experiments were done at two facilities. When a good determination of the base line was needed we used the ISIS pulsed muon facility at Rutherford Appleton Laboratory, UK. When high timing resolution was required we worked at the Paul Scherrer Institute, Switzerland (PSI). In μ SR experiments one injects polarized muons into the sample and applies a magnetic field. Decay positrons are emitted preferentially in the direction parallel to the muon spin and are detected by positron counters. We used two types of setups, the transverse field [TF] and the longitudinal field [LF], which also includes zero field, as shown in Fig. 2. The LF configuration works as in panel (a) in both facilities. The TF configurations work in ISIS as in panel (b) and at PSI as in panel (c). From the counters an histogram is generated of positrons counts as a function of time, where the time is measured from the moment the muons enter the sample. The asymmetries $A_{FB}(t)$, $A_{UD}(t)$ and $A_{LR}(t)$ are then generated by $A_{FB}(t) = [F(t) - B(t)] / [F(t) + B(t)]$ and similarly with U, D instead of F, B , where F, B, U, D are the forward, backward, up, and down counters. $A_{LR}(t)$ is generated only from the left counter in Fig. 2(c). Most of the data were taken with a ^4He cryostat. However, in order to study the internal field profile we had to avoid dynamical fluctuations by freezing the moments completely.

For this purpose we used the ^3He cryostat at ISIS with a base temperature of 350 mK. All μ SR measurements were done on sintered pellets.

II. TF- μ SR

These experiments are done by field cooling (FC) the sample to 1.8 K at an external field of 3 kOe in PSI and 400 Oe in ISIS. As explained above we apply the field perpendicular to their spin direction, and every muon then precesses according to the local field in its environment. When field cooling the sample, a vortex lattice is formed, and the field from these vortices decay on a length scale of λ . This leads to an inhomogeneous field distribution in the sample. Since the magnetic length scale is much larger than the atomic one, the muons probe the magnetic field distribution randomly, which, in turn, leads to a damping of the muons average spin polarization. This situation is demonstrated in Fig. 3 where we present an image of the field profile, and the corresponding the real and imaginary part of the muon asymmetry. At temperatures above T_c the field is homogeneous and all muons experience the same field, and therefore no relaxation is observed. Well below T_c there are strong field variations and therefore different muon precess with different frequencies, and the average polarization quickly decays to zero. In intermediate temperatures the field variation are not severe and the relaxation is moderate.

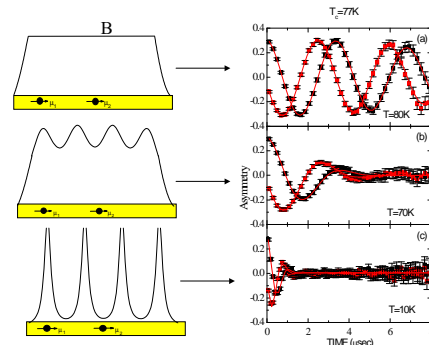


FIG. 3. Demonstrating the relation between the field distribution and the real and imaginary asymmetries in a TF- μ SR experiment. This data was taken at ISIS and is presented in a rotating reference frame.

It was shown that in powder samples of HTSC the muon asymmetry $A(t)$ is well described by⁹,

$$A(t) = \exp(-\sigma^2 t^2 / 2) \cos(\omega t + \varphi) \quad (1)$$

where $\omega = \gamma_\mu H$ is the precession frequency of the muon, σ is the relaxation rate, and φ is a phase which depends on the counters used to generate the asymmetry. Our analysis for both ISIS and PSI data is done in a reference frame rotating at ω_{rrf} and the real and imagi-

nary components of the signal are fitted simultaneously. Therefore, the frequency in Fig. 3 is $\gamma_\mu H - \omega_{rrf}$ where ω_{rrf} is chosen arbitrarily for presentation purpose. The solid line in this figure is the fit result. The fact that the whole asymmetry relaxes indicates that CLBLCO is a bulk superconductor.

The fit results for σ are shown in Fig. 4. As can be seen, the dependence of T_c on σ is linear in the underdoped region and universal for all CLBLCO families, as expected from the Uemura relations. However, there is a new aspect in this plot. There is no “boomerang” effect, namely, overdoped and underdoped samples with equal T_c have the same σ , with only slight deviations for the $x = 0.1$ sample as demonstrated by the arrows in Fig. 4. Therefore, in CLBLCO there is one to one correspondence between T_c and σ , and therefore λ_{ab}^{-2} , over the whole doping range. This is our first important finding.

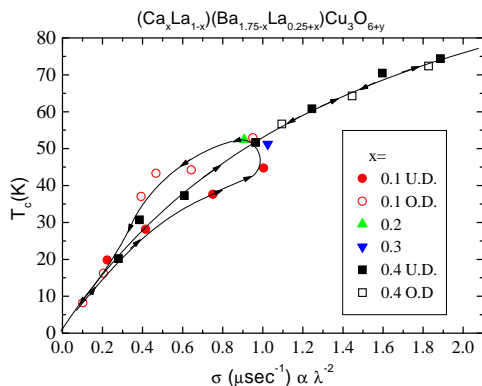


FIG. 4. A Uemura plot showing T_c vs. the muon relaxation rate σ in Eq. 1 for the CLBLCO family of superconductors.

III. ZF- μ SR

Typical muon asymmetry depolarization curves are shown in Fig. 5 (a) for different temperatures in the $x = 0.1$ and $y = 7.012$ ($T_c = 33.1K$) sample. The change of the polarization shape with temperature indicates a freezing process, and the data can be divided into three temperature regions. In region (I), given by $T \gtrsim 8$ K, the muon relaxes according to the well known Kubo-Toyabe (KT) function given by

$$KT(t) = \frac{1}{3} + \frac{2}{3}(1 - \Delta^2 t^2) \exp(-\frac{1}{2}\Delta^2 t^2), \quad (2)$$

(see Eq. 4) typical of the case where only frozen nuclear moments are present⁹. In region (II), bounded by $8 \text{ K} \gtrsim T \gtrsim 3 \text{ K}$, part of the polarization relaxes fast and the rest relaxes as in the first region. As the temperature is lowered the fast portion increases at the expense of the slow one. Moreover, the relaxation rate in the fast portion seems independent of temperature. Finally, at long time the asymmetry relaxes to zero. In region (III), where $3 \text{ K} \gtrsim T$, the asymmetry at long times no longer

relaxes to zero, but instead recovers to a finite value. This value is $\simeq 1/3$ of the initial asymmetry $A_z(0)$.

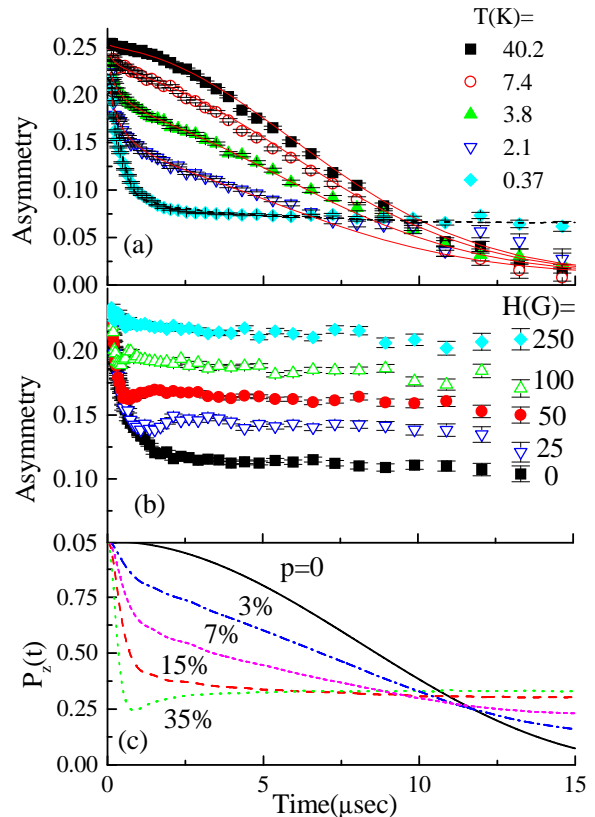


FIG. 5. (a) ZF- μ SR spectra obtained in a $x = 0.1$, $y = 7.012$ sample with $T_c = 33.1K$. The solid lines are fit to the data using Eq. 3, the dashed line is a fit using the simulation as described in the text. (b) μ SR spectra obtained in longitudinal fields from the $x = 0.4$, $y = 6.984$ sample at 350 mK. (c) Polarization curves generated by the simulation program as described in the text.

To demonstrate that the internal field is static at base temperature, the muon polarization was measured with an external field applied parallel to the initial muon spin-polarization. This geometry allows one to distinguish between dynamic and static internal fields. In the dynamic case the asymmetry is field independent¹⁰. In contrast, in the static case the total field experienced by the muon is a vector sum of H and the internal fields, which are of order $\langle B^2 \rangle^{1/2}$. For $H \gg \langle B^2 \rangle^{1/2}$ the total field is nearly parallel to the polarization. Therefore, in the static case, as H increases, the depolarization decreases, and the asymmetry recovers to its initial value. Because we are dealing with a superconductor, this field sweep was done in field-cool conditions. Every time the field was changed the sample was warmed to above T_c and cooled down in a new field. The results are shown in Fig. 5(b). At an external field of 250 G, the total asymmetry is nearly recovered. Considering the fact that the

internal field is smaller than the external one due to the Meissner effect, this recovery indicates that the internal field is static and of the order of tens of Gauss. Next we perform quantitative data analysis in two parts: high temperatures (region II), and base temperature.

A. High T Data Analysis

First we discuss region II. Here we focus on the determination of T_g . For that purpose we fit a combination of a fast relaxing function and a KT function to the data¹¹

$$A_z(t) = A_m \exp(-\sqrt{\lambda}t) + A_n KT(t), \quad (3)$$

where A_m denotes the amplitude of the magnetic part, λ is the relaxation rate of the magnetic part, and A_n is the amplitude of the nuclear part. The relaxation rate of the KT part was determined at high temperatures and is assumed to be temperature independent. The sum $A_m + A_n$ is constrained to be equal to the total initial asymmetry at high temperatures. The relaxation rate λ is common to all temperatures. The solid lines in Fig. 5(a) are the fits to the data using Eq. 3.

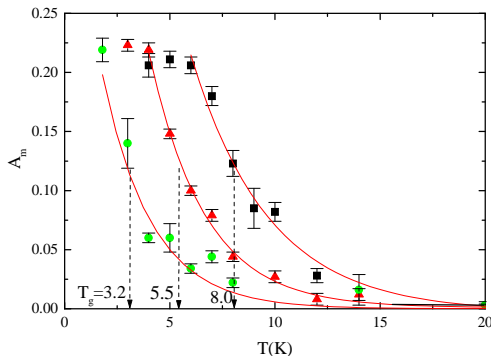


FIG. 6. Magnetic amplitude as function of temperature for different samples. The solid lines are guides to the eye.

The success of this fit indicates the simultaneous presence of two phases in the sample; part of the muons probe the magnetic phase while others probe only nuclear moments. As the temperature decreases A_m , which is presented in Fig. 6 for three samples, grows at the expense of A_n . At low temperatures A_m saturates to the full muon asymmetry. A similar temperature dependence of A_m is found in all samples. The origin of the magnetic phase is electronic moments that slow down and freeze in a random orientation. The fact that λ is temperature independent means that in the magnetic phase $\gamma_\mu \langle B^2 \rangle^{1/2}$, where γ_μ is the muon gyromagnetic ratio, is temperature independent. In other words, as the temperature is lowered, more and more parts of the sample become magnetic, but the moments in these parts saturate upon freezing.

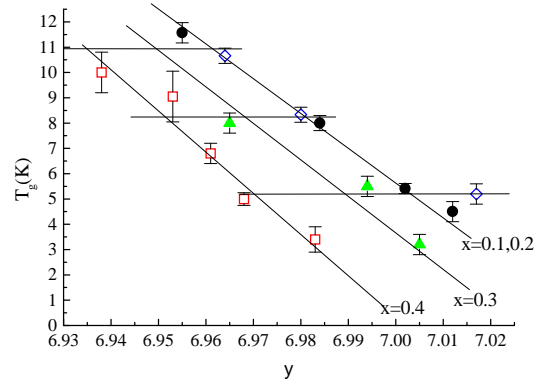


FIG. 7. T_g vs. y . The horizontal solid lines are the equal T_g lines appearing in Fig. 1.

Our criterion for T_g is the temperature at which A_m is half of the total muon polarization as demonstrated by the vertical lines in Fig. 6 for the three different samples. The phase diagram that is shown in Fig. 7 represents T_g for various samples differing in Ca and O contents. This diagram is systematic and rather smooth suggesting good control of sample preparation. As expected, for constant x , higher doping gives lower T_g .

We have singled out three groups of samples with a common $T_g = 11, 8$ and 5 K as shown in Fig. 7 by the horizontal solid lines. These samples are represented in the phase diagram in Fig. 1 by the dotted lines. The phase diagram, containing both T_g and T_c , is the second main finding of this work. It provides clear evidence of the important role of the magnetic interactions in high temperature superconductivity as discussed in Sec. V.

B. Low T Data Analysis

We now turn to discuss the muon depolarization at base temperature. In this case all the muons experience only a static magnetic field, as proven above. This allows one to reconstruct the internal field distribution out of the polarization curve. The polarization of a muon spin experiencing a unique field \mathbf{B} is given by $P_z(t) = \cos^2(\theta) + \sin^2(\theta) \cos(\gamma|\mathbf{B}|t)$, where θ is the angle between the field and the initial spin direction. When there is an isotropic distribution of fields, a 3D powder averaging leads to

$$P_z(t) = \frac{1}{3} + \frac{2}{3} \int_0^\infty \rho(|B|) \cos(\gamma|B|t) B^2 dB \quad (4)$$

where $\rho(|B|)$ is the distribution of $|\mathbf{B}|$. Therefore, the polarization is given by the Fourier transform of $\rho(|B|)B^2$ and has a $1/3$ base line. When the distribution of \mathbf{B} is centered around zero field, $\rho(|B|)B^2$ is a function with a peak at $\langle B \rangle$ and a width Δ , and both these numbers are of the same order of magnitude [e.g. Fig 8(b)]. Therefore we expect the polarization to have a damped oscillation and to recover to $1/3$, a phenomenon known as the dip

[e.g. the inset in Fig 8 (b)]. Gaussian, Lorentzian and even exponential random field distribution¹², and, more importantly, all known canonical spin glasses, produce polarization curves that have a dip before the 1/3 recovery. This is demonstrated in Fig. 9. For a Gaussian distribution of width Δ we obtain Eq. 4 which is demonstrated in panel (a). The cases of a canonical spin glass $\text{Fe}_{0.05}\text{TiS}_2$, and an extremely underdoped CLBLCO are presented in panels (b) and (c). Furthermore, a dipless polarization curve that saturates to 1/3 cannot be explained using dynamical arguments. Therefore, the most outstanding feature of the muon polarization curve at base temperature is the fact that no dip is present, although there is a 1/3 tail. This behavior was found in all of our samples with $T_c > 7$ K, and also in Ca doped YBCO¹³ and Li doped YBCO¹⁴.

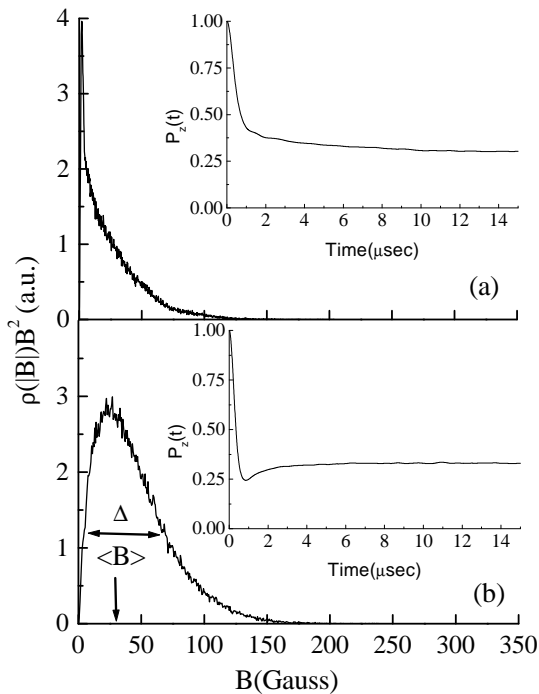


FIG. 8. (a) The internal field distribution extracted from the simulations for the case of correlation length $\xi = 3$ lattice constants, maximum moment size of $0.06\mu_B$ and magnetic moment concentration $p = 15\%$. Inset: The muon spin polarization for that distribution. (b) The same as above for the case of $p = 35\%$.

The lack of the dip in $P_z(t)$ can tell much about the internal field distribution. It means that $\langle B \rangle$ is much smaller than Δ . In that case the oscillations will be over-damped and the polarization dipless! In Fig. 8 we show, in addition to the $\langle B \rangle \simeq \Delta$ case described above [panel (b)], a field distribution that peaks around zero

[panel (a)]. Here $\langle B \rangle$ is smaller than Δ , and, indeed, the associated polarization in the inset is dipless. Thus in order to fit the base temperature polarization curve we should look for $\rho(|B|)B^2$ with most of its weight around zero field. This means that $\rho(|B|)$ diverges like $1/B^2$ at $|B| \rightarrow 0$, namely, there is abnormally high number of low field sites.

It also means that the phase separation is not a macroscopic one. If it were, all muons in the field free part would probe only nuclear moment and their polarization curve should have a dip or at least its beginning as in the high temperature data. The same would apply for the total polarization curve, in contrast to observation. Thus, the superconducting and magnetic regions are intercalated on a microscopic scale ($\sim 20\text{\AA}$)¹⁵. This is the third main finding of this work.

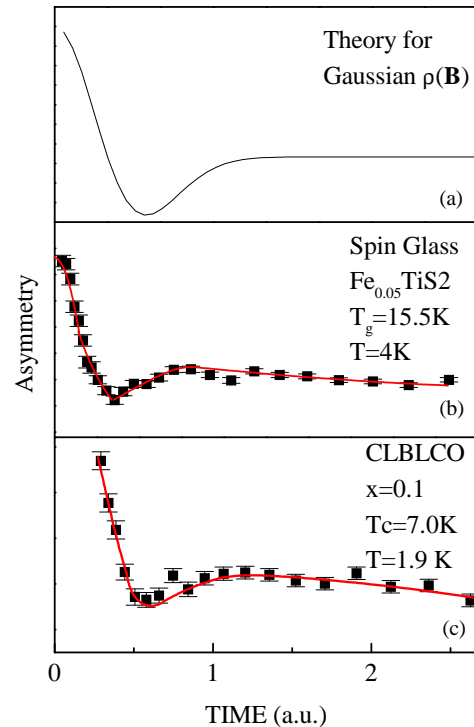


FIG. 9. Demonstrating the expected muon spin polarization function for (a) a Gaussian field distribution, (b) in a canonical spin glass $\text{Fe}_{0.05}\text{TiS}_2$, and (c) extremely underdoped CLBLCO.

The special internal field distribution, and the nature of the gradual freezing of the spins, can be explained by the intrinsic inhomogeneity of hole concentration. The part of the sample that is hole poor, and for that reason is “more” antiferromagnetic, will freeze, while the part which is hole rich will not freeze at all. The variation in the freezing temperature of different parts of the sample

can be explained by the distribution of sizes and hole concentration in these antiferromagnetic islands¹⁶. The large number of low field sites is a result of the fact that the magnetic field generated in the magnetic regions will penetrate into the hole rich regions but not completely.

IV. NUMERICAL SIMULATION

To improve our understanding of the muon polarization, we performed simulations of a toy model aimed at reproducing the results described above.

A 2D 100×100 square lattice is filled with two kinds of moments, nuclear and electronic. All the nuclear moments are of the same size, they are frozen and they point in random directions. Of the electronic moments only a small fraction p is assumed to be frozen; they represent magnetic regions with uncompensated antiferromagnetic interactions. Since these regions may vary in size, the moments representing them are random, up to a maximum size. The frozen electronic moments induce spin polarization in the other electronic moments surrounding them. Following the work of others¹⁸, we use decaying staggered spin susceptibility which we take to be exponential, namely,

$$\chi'(\mathbf{r}) = (-1)^{n_x+n_y} \exp(-r/\xi) \quad (5)$$

where $\mathbf{r} = n_x a \hat{x} + n_y a \hat{y}$ represents the position of the neighbor Cu sites, \mathbf{a} is the lattice vector, and ξ is the characteristic length scale. Because of this decay, at low frozen spin concentration, large parts of the lattice are practically field free (except for nuclear moments). However, the important point is that no clear distinction between magnetic and field free (superconducting) regions exists. This situation is demonstrated in Fig. 10.

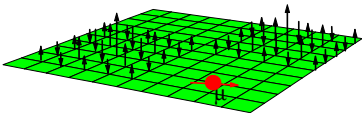


FIG. 10. Demonstrating the numerical simulations. Two spins (long arrows) are placed on the lattice. They polarize the near by spins. The muon interacts with the spin by dipolar interaction. Nuclear moment (which participate in the simulation) are not shown.

The muon polarization time evolution in this kind of field distribution is numerically simulated. The interaction between the muon and all the other moments is taken to be dipolar, and ξ is taken to be 3 lattice constants^{2,17}. The dashed line in Fig. 5 is a fit to the $T = 350$ mK data, which yield $p = 15\%$ and maximum moment size $\simeq 0.06\mu_B$. As can be seen, the line fits the data very well. However, as expected, the fit is sensitive to $p\xi^2$ only, namely the effective area of the magnetic islands, so longer ξ would have given smaller p . The field distributions and the polarization curve shown in Fig. 8 were actually generated using the simulation. In (a) the spin density is 15% while in (b) the density is 35%. In panel (c) of Fig. 5 we show the spin polarization for different hole concentration, varying from 0% to 35% with the same $\xi = 3$. The resemblance between the simulation results as a function of p and the muon polarization as a function of temperature in panel (a) leads us to our fourth conclusion that the freezing process is mostly a growth in the total area of the frozen AF islands.

V. DISCUSSION

We now discuss the phase diagram presented in Fig. 1. This diagram is consistent with recent theories¹⁹ of hole pair boson motion in an antiferromagnetic background. Those theories conclude that

$$T_c \propto J n_s \quad (6)$$

where n_s is the superconducting carrier density, and J is the antiferromagnetic coupling energy²⁰. Let us define $\Delta p_{hl} = p_{hl} - p_0$ where p_{hl} is the number of mobile holes and p_0 is the number of mobile holes at optimum.

We assume that

$$n_s(\Delta p_{hl}) = \frac{1}{2} (p_0 + \Delta p_{hl}) \quad (7)$$

and write

$$\Delta p_{hl} = K(x) \Delta y \quad (8)$$

where $\Delta y = y - 7.15$ is chemical doping measured from optimum, and K is a scaling parameter which relates Δy to Δp_{hl} . Since there is a linear dependence between T_g and chemical doping (Fig. 7) we predict that

$$T_g \propto J(1 - c_g n_s). \quad (9)$$

From Eq. 6 $T_c^{\max} \propto J n_s(0)$, therefore both T_c/T_c^{\max} and T_g/T_c^{\max} should be functions only of Δp_{hl} . This is demonstrated in Fig. 11(a). We find $K(x)$ by making all T_c/T_c^{\max} collapse onto one curve resembling the curve of $\text{La}_{2-x}\text{Sr}_x\text{Cu}_1\text{O}_4$ ²¹, where the exact doping is known. Using these values of $K(x)$ we also plot T_g/T_c^{\max} as a function of Δp_{hl} in Fig. 11(b). Again all data sets collapse onto a single line described by $T_g/T_c^{\max} = -3.1(2)\Delta p_{hl} - 0.21(2)$, or

$$T_g = 0.3T_c^{\max}(1 - c_g n_s) \quad (10)$$

with $c_g = 10.3$ when converting back to Eq. 9. This indicates that the same single energy scale J controls both the superconducting and magnetic transitions, and provides the exact n_s and T_c^{\max} dependence of T_g .

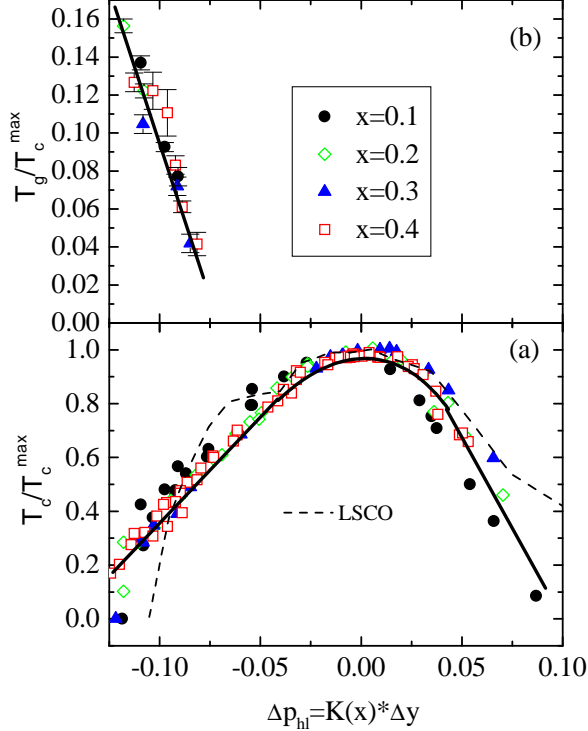


FIG. 11. T_c/T_c^{\max} and T_g/T_c^{\max} as a function of $K(x)\Delta y$ where $\Delta y = y - 7.15$, and $K(x)$ is chosen so that all T_c/T_c^{\max} data sets collapse to a single curve, which resembles the LSCO curve.

VI. CONCLUSIONS

We are now in a position to address the questions presented in the introduction. The Uemura relations is adequately respected for our HTSC “families”. We believe this is a result of the fact that there are no structural changes between the different “families”. The appearance of spontaneous magnetic field in CLBLCO is a gradual process. As the temperature is lowered microscopic regions of frozen moments appear in the samples, and their area increases but the moments do not. In the ground state the field profile is very different from that of a canonical spin glass or any other standard magnet. It could only be generated by microscopic intercalation of an abnormal number of zero field regions with magnetic regions without a clear distinction between the two.

Finally, and most importantly, the phase diagram containing both T_c and T_g leads us to believe that these temperatures are determined by the same energy scale.

VII. ACKNOWLEDGMENTS

We would like to thank the PSI and ISIS facilities for their kind hospitality and continuing support of this project. We acknowledge very helpful discussions with Assa Auerbach and Ehud Altman. This work was funded by the Israeli Science Foundation and the EU-TMR program.

-
- ¹ Y. J. Uemura *et al.*, Phys. Rev. Lett., **66**, 2665 (1991).
 - ² C. Howald *et al.*, cond-mat/0101251, J.M. Tranquada *et al.*, Nature **375**, 561 (1995); V.J. Emery and S.A. Kivelson, Physica C **209**, 597 (1993).
 - ³ J. I. Budnick *et al.* Europhys. Lett. **5**, 651 (1988) ; D. R. Harshman *et al.*, Phys. Rev. B **38**, 852 (1988); Ch. Niedermayer *et al.*, Phys. Rev. Lett. **80**, 4843 (1998).
 - ⁴ The density of hole per plane is $p = -0.205 + y/3$.
 - ⁵ O. Chmaissem *et al.*, Phys. Rev. B **63**, 174510 (2001).
 - ⁶ A. Knizhnik *et al.*, Physica C **321**, 199 (1999).
 - ⁷ A. Kanigel *et al.*, Phys. Rev. Lett. **88**, 137003 (2002).
 - ⁸ D. Goldschmidt *et al.*, Phys. Rev. B **48**, 532 (1993).
 - ⁹ *Muon Science: Muons in Physics, Chemistry and Materials*, Eds S. L. Lee, S. H. Kilcoyne and R. Cywinski (Institute of Physics, London), 1999.
 - ¹⁰ As long as $\gamma_\mu H < \nu$, where ν is the fluctuation rate.
 - ¹¹ A. T. Savici *et al.*, Physica B **289-290**, 338 (2000).
 - ¹² M. I. Larkin *et al.*, Phys. Rev. Lett. **85**, 1982 (2000); A. T. Savici *et al.*, Phys. Rev. B **66**, 014524, (2002).
 - ¹³ C. Bernhard *et al.*, Phys. Rev. B **58**, 8937 (1998).
 - ¹⁴ P. Mendels (private communication).
 - ¹⁵ A moment of $1\mu_B$ will induce a 1G field at a distance of $\sim 20\text{\AA}$. This field is equivalent to the nuclear moments background.
 - ¹⁶ J.H. Cho *et al.*, Phys. Rev. B **46**, 3179 (1992).
 - ¹⁷ B. Nachumi *et al.* Phys. Rev. Lett. **77**, 5421 (1996); S. H. Pan *et al.*, Nature **401**, 746 (2000).
 - ¹⁸ A. J. Millis, H. Monien, and D. Pines, Phys. Rev. B **42**, 167 (1990); J. Bobroff *et al.*, Phys. Rev. Lett. **79**, 2117 (1997); M. H. Julien *et al.*, Phys. Rev. Lett. **84**, 3422 (2000).
 - ¹⁹ S. C. Zhang *et al.*, Phys. Rev. B **60**, 13060 (1999); E. Altman and A. Auerbach, Phys. Rev. **B65**, 104508 (2002).
 - ²⁰ Y. J. Uemura *et al.*, Phys. Rev. Lett. **62**, 2317 (1989); V. J. Emery and S. A. Kivelson, Nature **374**, 434 (1995).
 - ²¹ C. Panagopoulos *et al.*, cond-mat 0204106.